Q. J. R. Meteorol. Soc. (2004), **130**, pp. 2991–3014 doi: 10.1256/qj.03.190

Boundary-layer variations due to orographic-wave breaking in the presence of rotation

By B. GRISOGONO[1]* and L. ENGER[2]

[1]*Department of Geophysics, Zagreb University, Croatia*
[2]*Department of Earth Science, Uppsala University, Sweden*

(Submitted: 29 September 2003; revised 24 June 2004)

SUMMARY

A mesoscale numerical model is used to study the atmospheric boundary-layer (ABL) response to nonlinear orographic forcing with Coriolis effect, f, over a mountain with length (the cross-wind component) comparable to the Rossby radius of deformation, L_R. The orographic-wave breaking occurring for Froude number $Fr < 1$, affected by $f > 0$, intensifies on the northern flank for westerly flows, as also found in other recent studies. A cumulative effect occurs as the Coriolis force lifts the northern ABL top and generates a stronger low-level jet (LLJ) than on the southern side. A differential layering also appears, since the specific humidity is higher in the lower southern ABL than in the related northern ABL, and vice versa. By contrast, there are higher values of the turbulent kinetic energy and humidity in the upper northern ABL.

The breaking of flow symmetry around the orography due to f changes both the vertical vorticity and horizontal divergence field, (ζ, D), it modulates eddies and turbulence leading to the differential layering of the ABL. The stronger northern LLJ and its weaker southern counterpart, both meandering, together with the asymmetric wave breaking, induce strong lee-side fluctuations of the (ζ, D) field in the presence of f. The enhanced (ζ, D) production due to wave breaking over the distance $\approx L_R$, the primary atmosphere–orography resonance occurs mainly in the vertical, while the 'f-enhancement' occurs in the horizontal plane. In this way, the initial mesoscale forcing may extend its effects over the synoptic scale.

KEYWORDS: Jet Numerical modelling Resonance Turbulence

1. INTRODUCTION

(*a*) *Overview*

The importance of atmospheric buoyancy waves on essentially all relevant atmospheric scales has been revealed during the last three decades or so. Simultaneously there have been many recent advances in studying nonlinear buoyancy waves where a resonance between the flow and orography may take place (e.g. Peltier and Clark 1979; Pierrehumbert and Wyman 1985; Smith 1985, 1989; Durran 1999; Nappo 2002). While the main interaction between two-dimensional (2D) nonlinear buoyancy waves and the mean flow (local 'supercriticality', elevated flow stagnation and eventual hydraulic jump) is essentially captured by nonlinear hydraulics, as shown by Smith (1985, 1987) and Klemp and Durran (1987), the nonlinear 3D flow structures are richer and not yet fully explored. The cornerstone of the 3D atmospheric linear buoyancy-wave theory is provided by Smith (1980); this is extended for variable background flow by Grubišic and Smolarkiewicz (1997), Shutts (1998), Broad (1999) and others. Miranda and James (1992) and Smith and Grønås (1993) address numerically 3D nonlinear buoyancy waves, their breaking and the flow splitting. Ólafsson and Bougeault (1996), Schär and Durran (1997) and Bauer *et al.* (2000) continue and expand their work, exploring more fully the parameter space of nonlinear airflow over orographies, including wave breaking, eddy shedding, etc. Fritts *et al.* (1994) in a series of papers study similar 3D processes but sufficiently far from the ground surface. Most of these studies neglect the Coriolis parameter (f) and surface friction effects, but reveal the essential importance of 3D effects on the lateral deflection of the flow, wave-breaking positions and intensities, and upstream influences.

* Corresponding author: Department of Geophysics, Zagreb University, Croatia. e-mail: bgrisog@gfz.hr

Ólafsson and Bougeault (1996, 1997) and Bauer *et al.* (2000) use higher-order closures for turbulence parametrizations in their simulations. Epifanio and Durran (2001) use only a first-order closure with a fixed Prandtl number equal to one. Nevertheless, they largely agree with the former results, in addition to new ones (e.g. a lee-slope buoyancy enhancement in 3D while the wave amplitude decreases compared to the 2D runs, and an increase in flow deflection due to wave breaking—related to the upstream propagating columnar disturbances forced by the high-drag state). Although a higher-order closure is not essential to study 3D nonlinear mountain airflow, it seems to be a desirable feature if one wants to relate the latter (e.g. flow deflections) with variations in the atmospheric boundary layer (ABL). This is also in accordance with Ding *et al.* (2003) who use large-eddy simulations (LES) to address strongly stratified flow over a 3D hill with $f = 0$.

Studies of nonlinear waves often take a perspective either from the waves towards the larger scale ignoring or oversimplifying friction and turbulence, or towards the smaller scale thus often neglecting f. In other words, the nonlinear buoyancy waves are seldom addressed from both large- and small-scale perspectives simultaneously, which appears to be an important but not well explored area (Trüb and Davies 1995). Finally, Ólafsson and Bougeault (1997) studied the combined effect of $f \neq 0$ and surface friction on wave drag; the reported drag is suppressed and linear theory applies better than expected. These are more concerned with integrated effects; however, details of the ABL responses and feedbacks remain to be studied. Hunt *et al.* (1997) attempted an asymptotic multi-layer analysis of nonlinear airflow over mountains (including wakes, wind curvature, etc.). The importance of the barrier jet due to $f \neq 0$ is mentioned. Moreover, Hunt *et al.* (2001) address the latter more specifically via an asymptotic analysis substantiated by relevant numerical simulations. They show that the Coriolis force induces rising of the westerly flow from the northern flank of the barrier and descending flow from the southern flank. This effect appears strongest when the characteristic barrier length, $2L_y$, is comparable to the internal Rossby radius of deformation, L_{R}. Hence, an additional resonance between the flow and orography may occur: one stronger and already implied in the vertical plane inducing wave breaking; and one weaker in the horizontal plane causing differential vertical deflections. These two together are called here, perhaps controversially, a double-resonance phenomenon (DRP).

Ólafsson (2000) studies drag asymmetries with respect to nonlinear rotational flows. Even without friction, he finds essential mesoscale ingredients for the flow asymmetry as in his collaborative work with Hunt *et al.* (2001). His results indicate that more vigorous wave activity takes place in a rotational blocked flow on the left lee side of the orography (looking downwind). This is related to the amount of the blocking and f. None of the work cited pays much attention to internal variations of the ABL induced by the divergence–vorticity excitation due to wave breaking in the presence of rotation. That comprises the aim of this study.

(*b*) *Background*

The principal parameters in many of the above studies and in this work are the 'vertical' Froude number and Rossby number:

$$\begin{aligned} Fr &\equiv U/(NH), \text{ and} \\ Ro_x &\equiv U/(fL_x), \end{aligned} \tag{1}$$

respectively. Here U and N are the background (usually prescribed) constant wind speed and buoyancy frequency, respectively, H is the maximum orography height and L_x

is one of the two characteristic horizontal scales (mountain half-width). An additional Rossby number is defined in terms of the perpendicular 'half-length', L_y, and the lateral velocity scale, V; thus,

$$Ro_y \equiv V/(fL_y), \tag{2}$$

as in the semi-geostrophic theory (e.g. Holton 1992). Such a mesoscale concept has already been applied successfully, e.g. in coastal meteorology (Overland 1984; Cui *et al.* 1998) where coastal jets and hydrodynamically steep coastal airflows are ubiquitous features (e.g. Grisogono and Tjernström 1996; Tjernström and Grisogono 1996). Consequently, some of the main conclusions from Hunt *et al.* (2001) can be expressed in terms of (1) and (2). The mentioned DRP will preferably occur when $Fr < 1$, $Ro_x \gg 1$, while the (internal) Rossby radius of deformation, expressed either as $L_R = NH/f$ (e.g. Hunt *et al.* 2001) or $L_R = 1.5U/f$ (e.g. Epifanio and Durran 2001), relates to L_y, namely $L_R \approx 2L_y$. The same parametric subspace of the DRP may be re-defined via the large Burger number (e.g. Lesieur 1997), $Bu = (Ro_x/Fr)^2$, meaning hydrodynamically steep orography in a rotating flow while keeping $Fr \leqslant 1$ and $L_R \approx L_y$.

Besides wave breaking, the $Fr < 1$ nonlinearity induces piling up of the windward air mass which senses if $L_R \approx 2L_y$. This yields to the preferential flow side governed by the Coriolis force, a sort of semi-geostrophic partial adjustment yielding the orographic low-level jet (LLJ) as in e.g. Hunt *et al.* (1997, 2001). Such a wind speed increase of, say, 10–25% on the northern side, compared to that on the southern side where a weaker LLJ occurs further downstream, will first destabilize dynamically the northern upper part of the ABL. Based on this, and because rotation affects wind more than temperature (e.g. Smith 1982), one may expect that the northern lee side exhibits a relatively smaller positive Richardson number, Ri, than the southern lee side, reflecting the state of the ABL. Consequently, the ABL in the lee would vary significantly not only in the streamwise, but also in the lateral (north–south) direction as will be shown here.

This study builds on ideas from Ólafsson and Bougeault (1997) , Bauer *et al.* (2000), Epifanio and Durran (2001) and Hunt *et al.* (2001). The focus here is on the dynamic features less explored in their studies, such as the LLJ and the ABL. The dynamic interplay among the orographic-wave breaking, the induced jet, and the ABL leads to a mixing asymmetry in the lee wake(s) in the lower troposphere having a synoptic streamwise scale up to 1000 km (Hunt *et al.* 2001). The latter scale transition from the mesoscale to the synoptic scale might be due to the DRP. It is at $Fr \approx 0.6$ that Ding *et al.* (2003) find the relatively largest drag coefficients (their Fig. 17); once again, this study focuses on the same Fr but with $f \neq 0$. Mapping out the LLJ north (stronger) and south (weaker) of the orography (for $U > 0$ and $f > 0$), in relation to the differential layering of the ABL in the lee, will indicate important possible consequences for e.g. tracers, clouds and air chemistry. These dynamic features are important in reality, where they inevitably appear more complex. As such, they may greatly affect the passage of fronts, precipitation patterns, etc. (e.g. Egger and Hoinka 1992; Thorpe *et al.* 1993; Hunt *et al.* 1997). This might also be a partial explanation for the spatial variability of the bora wind along the eastern Adriatic coast (e.g. Ivancan-Picek and Tutiš 1996; Brzovic 1999) in addition to the upstream flow preconditioning.

To recap: the aim of this study is to map out the ABL spatial variations in the presence of localized wave breaking and the Coriolis effect. While the former, the orographic-wave breaking, is nonlinear, the latter is a linear phenomenon; hence, their combination is strictly a nonlinear feature yielding some unexpected variations in the ABL. Needless to say, these ABL variations are usually not well captured in current numerical weather prediction (NWP) models or climate models.

2. THE NUMERICAL MODEL

(*a*) *Overview*

A nonlinear, 3D, hydrostatic, constant f-plane model with a higher-order closure turbulence parametrization scheme is used (Tjernström *et al.* 1988; Andrén 1990; Enger 1990). This so-called MIUU model solves five prognostic equations: two for the horizontal wind, and one each for potential temperature (Θ), specific humidity and turbulent kinetic energy (TKE), and many diagnostic equations each time step. A more detailed set-up is reported in Grisogono (1995), Arya (1999) and Abiodun and Enger (2002), among others, thus further details are not given here. A good advection scheme is essential for studying orographic wave breaking; here an upstream explicit scheme $O((\Delta x)^3, (\Delta t)^3)$, where t is time, is used (Enger and Grisogono 1998). The model has been checked against observations, linear theories, measurements and other numerical models, in a few tens of articles, e.g. Holmgren (1994) and Tjernström and Grisogono (2000). The model's best properties are nonlinearity, 3D capability and an economic but still faithful treatment of turbulence. For instance, Abiodun and Enger (2002) show with this model that dispersion from point sources in the convective ABL—a plume ascending, descending and possibly splitting—is due to the interplay between the nonlinear advection and diffusion. This phenomenon was misinterpreted for about 25 years prior to their recent finding. Söderberg and Tjernström (2002) use the same model to explain a transient spatio–temporal behaviour of a coastal jet, i.e. a diurnally trans-critical flow in a marine ABL in the presence of a mountainous coast.

The only modification made but not described in the above mentioned papers is an improvement in the turbulence length scale, λ_{turb}, under stable stratification. It is based on Hunt *et al.* (1988), Tjernström (1993) and Schumann and Gerz (1995):

$$\lambda_{\text{turb}} = \text{const}(TKE)^{1/2} \min(1/n,\ 1/\$), \tag{3}$$

where *TKE* is the local TKE calculated prognostically, n is the local N and \$ is the local absolute vertical shear of the mean wind (const ≈ 0.5). Equivalently, λ_{turb} in (3) can be expressed in terms of the local gradient *Ri*, instead of n and \$ (e.g. Grisogono and Oerlemans 2002). The model employs no explicit numerical diffusion, a desirable property related to the class of advection schemes used (e.g. Durran 1999).

(*b*) *Model set-up*

The model employs 121×101 horizontal grid points in x, y coordinates, having constant $\Delta x = 2.5$ km and $\Delta y = 5$ km increments, with a terrain-influenced vertical z coordinate. For most of the results discussed, there are 36 grid points in the vertical distributed log–linearly starting with $\Delta z_{\text{MIN}} = 4$ m from the surface and becoming almost constant above the first kilometre. This yields the largest depth interval, $\Delta z_{\text{MAX}} \approx 500$ m, near the model top which is at 15 km; the last 5 km occupies a sponge layer. The time step is 20 s. An occasional $2\Delta t$ time filter is used (every 20 time steps in this study). The zero-level surface is kept at 280 K, so that all transiences or intrinsic unsteadiness arises from interplays between orographic waves, the LLJ and turbulence. The 3D model is abruptly forced at time zero with the given constant background flow and orography input, similar to that in e.g. Bauer *et al.* (2000), to radiate out transient perturbations related to a sort of geostrophic adjustment approaching a more balanced state, as determined by a 3D mountain flow. This latter is not necessarily a steady state, depending on the importance of nonlinear processes involved (e.g. Grisogono 1995). The model's lateral and upper boundary conditions are designed to minimize reflections, while 'no-slip' is the lower boundary condition. The five first and last lateral grid points

use a first-order forward-upwind advection scheme on which a 'constant inflow–gradient outflow' condition is applied; moreover, a weak additional lateral diffusion is used. For the upper part of the sponge layer the same dissipative advection scheme is employed (instead of $O((\Delta x)^3, (\Delta t)^3)$ as default). The domain and the duration of simulations are based on the arguments of Epifanio and Durran (2001). They stress the importance of both domain size and duration of simulations in order to prevent the overall results being sensitive to spurious reflections; R. Smith (personal communication, 1999) emphasized that independently. The results, stored and checked for each hour, are reported after 20 h of the simulations (see below).

3. Simulations

(*a*) *Background*

Simulations are designed so that, at least qualitatively, they can be compared to some subsets of those performed by Ólafsson and Bougeault (1996, 1997), Bauer *et al.* (2000), Ólafsson (2000), Epifanio and Durran (2001) or Hunt *et al.* (2001) . The simulations are organized with respect to a subspace of (1); namely, so that $Fr \approx O(1)$ and $Ro_x \geqslant O(1)$ or $Ro_x \gg O(1)$.

The stated model set-up is true for most of the runs to be presented 20 hours from the start. The 20 h of simulations, t_{MAX}, corresponds to 57.6 dimensionless time units ($= U \cdot t_{MAX}/L_x$) to enable the results to be compared with the other studies. Some of the simulations are also performed with the horizontally stretched 'telescopic' grid, which starts with the mentioned grid lengths (Δx, Δy) only in the centre, thus additionally avoiding any possibly significant spurious lateral reflections, and testing for the extent of lee-side eddy-shedding found by Hunt *et al.* (2001). For these simulations the horizontal domain extends from 10% up to several 100% in each direction. The results from these runs over an extended domain agree reasonably well with the first ones to be presented here. Also, tests adding more grid points, and refining spatial and temporal resolution are performed; all these confirm that the chosen model set-up is appropriate for this study. However, for the $Fr = 2$ regime, with a high vertical wavelength, the model top was lifted to 26 km starting with the sponge layer at 13 km, and several more vertical grid points were added. This set-up adjustment, although inducing only minor changes in the calculated field values when compared to the default set-up, was made in order to be on the safe side regarding the modelled wave dynamics (Klemp and Lilly 1978; Grisogono 1995). The vertical resolution was sufficient with eight grid points or more per dominant orographic-wave length (e.g. Enger and Grisogono 1998; Durran 1999). An elongated, laterally stretched Gaussian orography is given by the half-width $L_x = 10$ km along the flow and the half-length $L_y = 50$ km perpendicular to the flow; the maximum height is $H = 1000$ m along $x_0 = 90$ km:

$$\begin{aligned} h_M(x, y) &= H \exp[-\{(x - x_0)/L_x\}^2] \quad \text{for } -L_y/2 < y < L_y/2, \\ \text{and } h_M(x, y) &= H \exp[-\{(x - x_0)/L_x\}^2 \\ &\quad - \{(y - L_y/2)/(L_y/2)\}^2] \quad \text{elsewhere.} \end{aligned} \tag{4}$$

The background flow is constant westerly, $U = 8$ m s^{-1}. The flow regime with respect to the wave linearity is entirely controlled by N which is either 0.004 or 0.0132 s^{-1}, basically excluding buoyancy–inertia waves. Consequently, the primary hydrostatic orographic wave has its characteristic dimensions roughly 20 km × 100 km × λ_z, where λ_z is the vertical wavelength ($= Fr \cdot 2\pi H$). The hydrostatic assumption is

TABLE 1. THE SIMULATION SET-UP AND PARAMETER SPACE STUDIED

	Latitude ϕ (°N)			
	0	10	45	80
Froude number	Rossby number			
2.0	∞	32	7.6	5.6
0.6	∞	32	7.6	5.6

The principal (along-flow) Rossby number $Ro_x = U/(fL_x)$, and Froude number $Fr = U/(NH)$, are given. The background wind of 8 m s^{-1} is westerly and stratification, N, is 0.004 s^{-1} or 0.0132 s^{-1}, thus there are two vertical wavelengths, $Fr \cdot 2\pi H$. The terrain maximum height $H = 1$ km, the half-width along the flow $L_x = 10$ km, the perpendicular 'half-length' $L_y = 50$ km, H is kept over $-L_y/2 < y < L_y/2$ at $x_0 = 90$ km; see (4) for h_{M}. See text for further details.

valid as $U/(NL_x) \ll 1$ (like a 'horizontal' Fr). Wherever (4) drops to 20 m or less ($\leqslant 2\%$ of H) it is set to zero. The first grid point is set to constant roughness length everywhere $z_0 = 0.1$ m; the mean wind is zero at z_0.

The ABL height, h, can be defined as that where the along-stream wind speed, U, approaches (first time from below) 90% of its background speed; in our case this is the height h_U corresponding to 7.2 m s^{-1}. This may be so away from the mountain, but this simple definition, $h = h_U$, is useless in a complicated flow with wave breaking. The surface-inversion height could be used instead, if it exists, but this is often very sensitive which limits the vertical temperature gradient that can be used (e.g. Mahrt 1998). A more sophisticated option is $h = h_{TKE} \propto \langle TKE^{1/2} \rangle / |f|$ for $f \neq 0$ with the angle brackets representing a vertical average (see more in e.g. Stull 1988). If the specific humidity decreases with height and may be treated as a passive tracer, it can be used for defining h, the height where a certain fraction of the near-surface specific humidity is reached. This fraction is chosen here to be 1.1 g kg^{-1} corresponding to h_U away from the orography under weakly nonlinear $f = 0$ conditions. Partly based on our marine and coastal-mountain work (Rogers *et al.* 1998; Tjernström and Grisogono 2000), and more especially the way the specific humidity is treated here, we chose this humidity as a reliable ABL indicator. This h should often correspond to that from h_{TKE} when a suitable proportionality is chosen.

Setting the model input so that no condensation/evaporation takes place in the flow means that the specific humidity, a prognostic field in the model, behaves nearly as a passive tracer (neglecting weak effects on buoyancy). The input sets it to decrease linearly from the surface, i.e. 3 g kg^{-1}, to almost zero at the model top. The specific humidity is used here to map the ABL. Two sets of simulations are presented: nearly linear and strongly nonlinear. Within each of these only latitude varies, $\phi = 0$, 10, 45 and 80°N or, equivalently, setting $Ro_x = \infty$, 32, 7.6 and 5.6. These numerical experiments are summarized in Table 1.

Finally, more attention is given to the case $(Fr, \phi) = (0.6, 45°)$.

(*b*) *Nearly linear regime, Fr = 2 with varying* ϕ

The following results serve for comparisons with the other studies cited, in order to put this work into perspective and to be able to follow consecutive changes in the

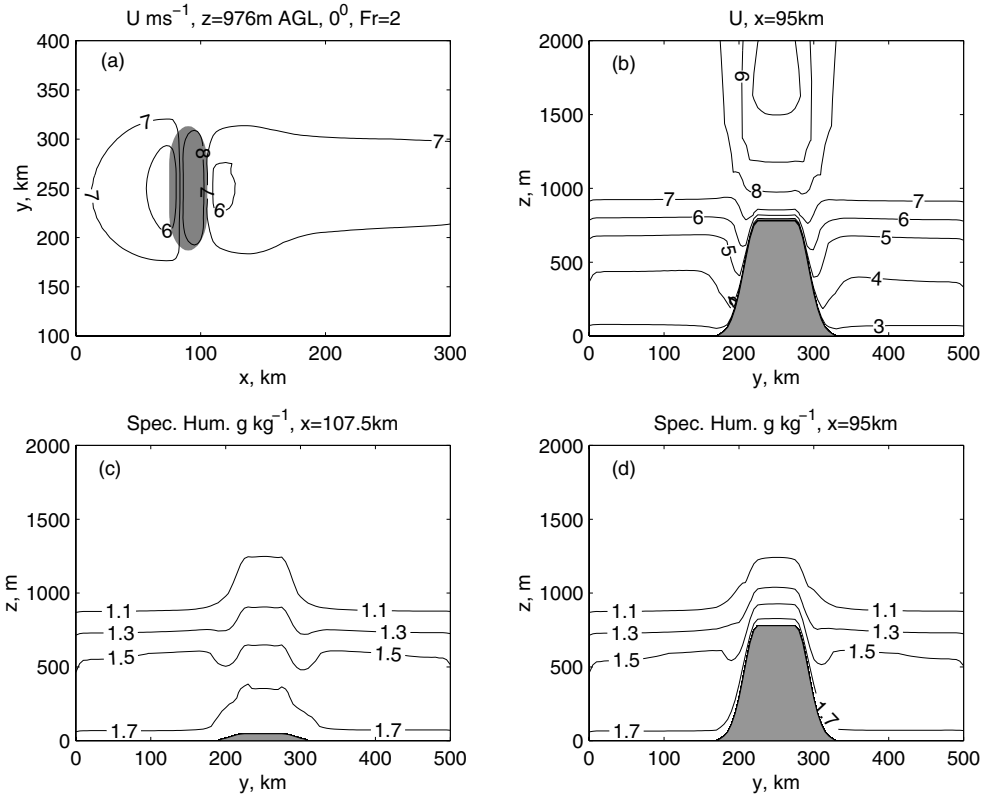

Figure 1. Airflow with Froude number $Fr = 2$, Rossby number $Ro_x \to \infty$ ($\phi = 0$) after 20 h: (a) The U component, from left to right, 976 m above ground level (AGL), the mountain is shown shaded in light grey from 100 m to its 1000 m top at $x = 90$ km, see (4); (b) the U component, towards the reader, at $x = 95$ km, 5 km behind the mountain top; (c) same as (b) but for specific humidity at $x = 107.5$ km; (d) same as (c) but at $x = 95$ km (to be related to both (b) and (c)). The U isolines are at 1 m s^{-1} intervals, the humidity isolines are in steps of 0.2 g kg^{-1}. The set-up is outlined in Table 1.

governing parameters, Fr and Ro_x. This flow belongs to a weakly nonlinear (or nearly-linear) regime (e.g. Smith 1980; Thompson *et al.* 1991).

A run with $f = 0$ ($\phi = 0$, $Ro \to \infty$) is briefly discussed first. A horizontal cross-section of the along-flow component, U, at height $z = 967$ m is shown in Fig. 1(a); its vertical cross-section 5 km behind the mountain top is in Fig. 1(b), while the related specific humidity is in Fig. 1(d); the same humidity 12.5 km downstream is shown in Fig. 1(c). The flow is nearly steady and is almost perfectly symmetrical in the (x, y) and (y, z) planes about the orography h_{M}. Earlier studies also found no flow-reversal in this regime (Ólafsson and Bougeault 1996; Bauer *et al.* 2000). No corresponding reversals appeared in Epifanio and Durran (2001) either, but they simulated a moderate enhancement of the normalized drag coefficient and an increase of about 50% in fractional mass deflection compared to linear theory (their Figs. 2(a), 3 and 6).

Since h was chosen here to correspond to 1.1 g kg^{-1}, the mean $h \approx 800$ m for $x \geqslant 95$ km, except in the lee 200 km $\leqslant y \leqslant$ 300 km where h exhibits variations. This h is close to the heights where $\partial(TKE)/\partial z$ approaches zero determining the value of h_{TKE} and h_U, except over the terrain and in the lee. Hence, these estimated heights for the ABL agree in the area $x > 95$ km, $y < 200$ km and $y > 300$ km. At higher levels

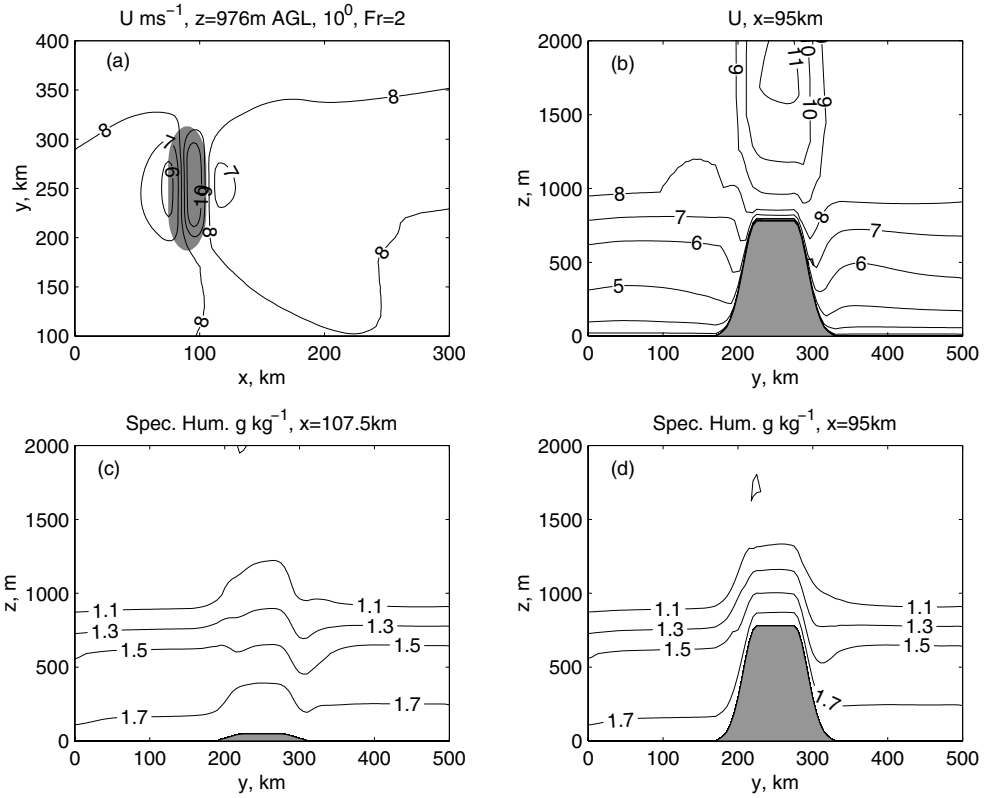

Figure 2. Same as Fig. 1 but for $Ro_x = 32$ ($\phi = 10°$).

than presented in Fig. 1, there is a nearly linear wave signature, namely the parabolic pattern formed by $y \approx (NL_x xz/U)^{1/2}$ as shown by Smith (1980). This run is the least perturbed one. If the orography were slightly warmer than the surrounding air, yielding an unstable surface layer, it would produce in the lee a flow reversal and a vortex pair stretching more than 100 km off the mountain (not shown; found—thanks to one of the referees).

Figures 2 to 4 display equivalent flows at $\phi = 10°$, 45° and 80° respectively. A moderate overall flow distortion is apparent. Somewhat higher wind speeds in the lee and behind the northern flank occur as f increases. The flow becomes moderately dispersed and less symmetrical with increasing ϕ. The specific humidity in Figs. 1 to 4, shows that the bulk of the ABL remains essentially the same for various ϕ, again with the exception of in the lee area.

The U cross-sections suggest that the bulk of the ABL would gradually sink with increasing ϕ; using h_U, h sinks from 900 to less than 300 m. This result is in accord with Smith (1982) showing that f mainly affects the (U, V) and less the other fields. Hence, the specific humidity south and north of h_M is less affected, and the related h changes only a little. It is not of course expected that h_U and h would correspond in the lee. It is known that in most conditions $f \neq 0$ has a stabilizing effect on geophysical flows (e.g. Pedlosky 1987; Holton 1992); also, the tropospheric depth decreases with increasing f. Because the maxima of U and h_U occur at lower heights with increasing f, and

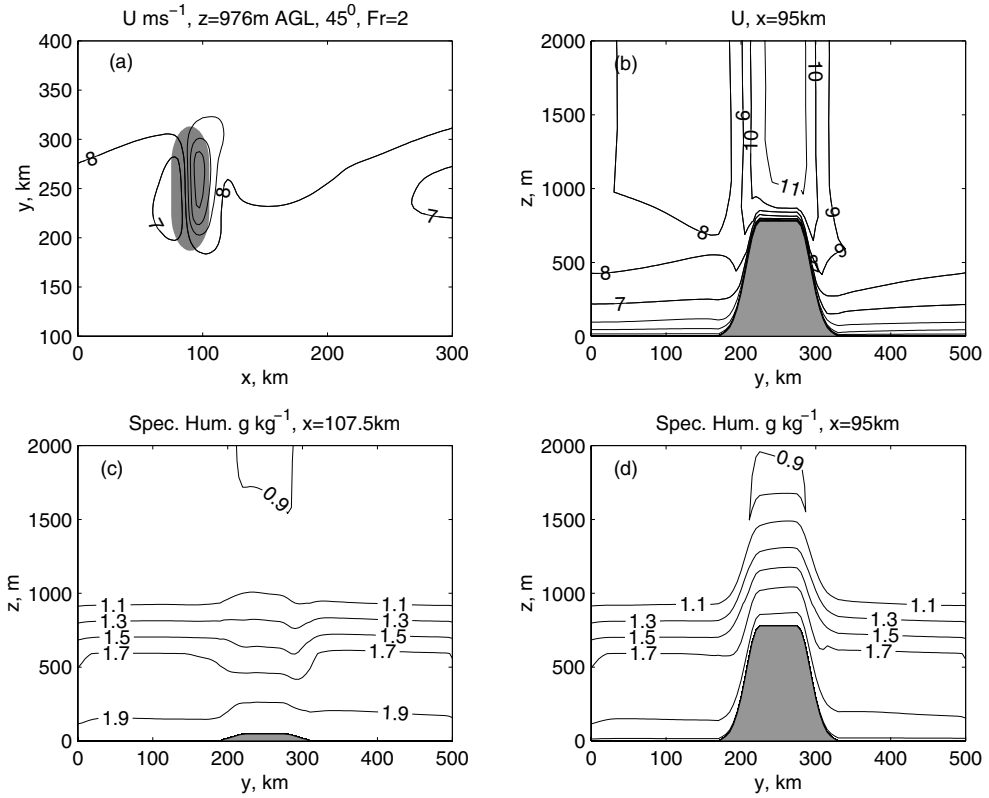

Figure 3. Same as Fig. 1 but for $Ro_x = 7.6$ ($\phi = 45°$).

the related TKE production grows with roughly ^{2} if the eddy diffusivity, K_m, does not change, the ABL's ratio $\langle TKE^{1/2}\rangle/|f|$ would remain nearly constant with ϕ, and so does h. But K_m will also increase if there is enough shear and then $\langle TKE^{1/2}\rangle/|f|$ and h will change (see following subsections with $Fr = 0.6$). At higher levels, besides minor wave-field dispersion and the northern lee-side acceleration due to $f > 0$, the linear flow pattern is similar to that for $\phi = 0$.

(*c*) *Nonlinear regime, Fr = 0.6 with varying φ*

Wave breaking and significant lee-side vortex activities take place in a nonlinear regime with $Fr = 0.6$ and varying ϕ. Figures 5 to 8 are organized in a similar way to Figs. 1 to 4.

Figure 5 relates to the somewhat blocked, high-drag regime (e.g. Ólafsson 2000) exhibiting various intensities in its upstream columnar disturbances (e.g. Baines 1995). The flow regime relates to vigorous vortex shedding (Smith 1989; Schär and Smith 1993; Schär and Durran 1997) induced by the presence of two hydraulic jumps over the flanks of the orography. These two jumps are unsteady, undergoing quasi-periodic motions back and forth, left and right, while also somewhat changing in their intensities, depending on the nonlinear advection and turbulent diffusion. A third wave-breaking area is in the immediate lee, somewhat similar to the situation in 2D simulations (e.g. Enger and Grisogono 1998). With increasing f, Figs. 6, 7 and 8, the wave-breaking regions become more interconnected and fluctuating in time. They occupy essentially

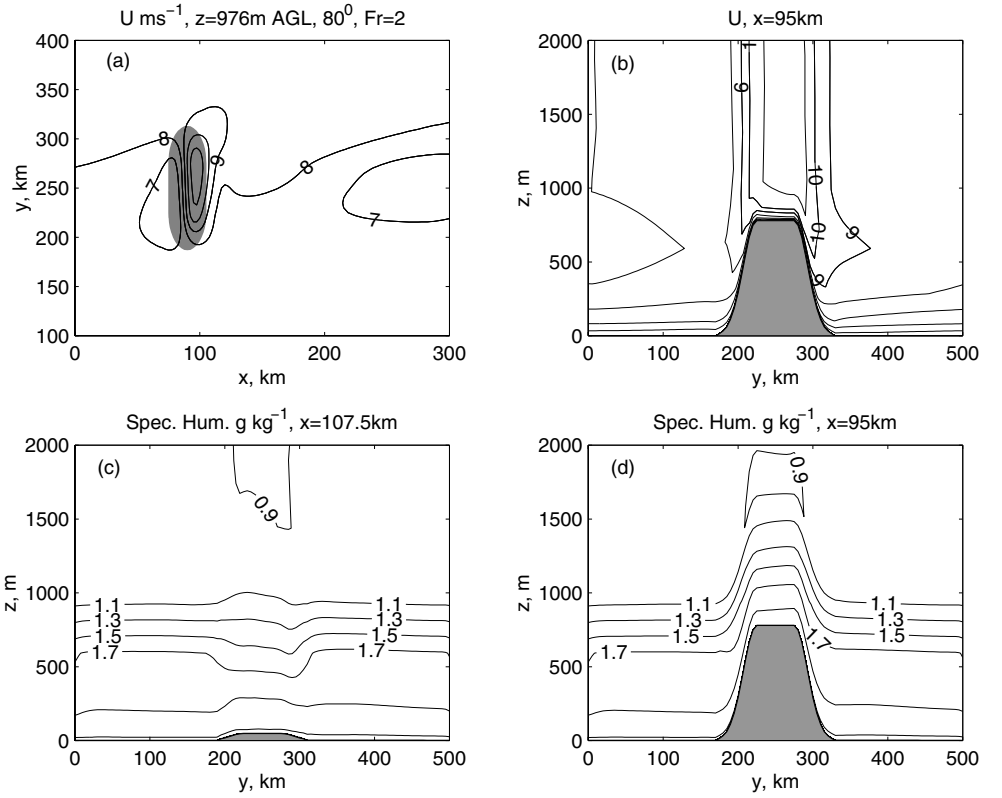

Figure 4. Same as Fig. 1 but for $Ro_x = 5.6$ ($\phi = 80°$).

the whole lee side and the parts of the flanks roughly making $2L_y + 2(L_x/2) \approx L_R$. Figure 6 reveals slight differential layering of the lee-side ABL north and south from the orography. That becomes more apparent in Fig. 7 and more vigorous in Fig. 8; the flow symmetry around $y = 250$ km is broken completely. The meandering LLJ becomes obvious (Figs. 7 and 8). With $f > 0$, both the upwind deceleration and the downwind acceleration move off the symmetry line $y = 250$ km; the former moves south, and the latter moves north, which is in accord with Smith (1982) and Pierrehumbert and Wyman (1985). Breaking this symmetry allows for enhanced exchange of wind velocity components, and consequently more intense velocity gradients. This preferential advection also facilitates a more vigorous wave breaking near to the northern flank as in Ólafsson (2000, his Fig. 8) and Hunt *et al.* (2001). Moreover, the maximum and minimum of the V-component tilt off of the horizontal plane: the southern minimum V lifts up and the northern maximum V sinks down with $f > 0$ (not shown). The northern LLJ around the ABL-top reaches 14–15 m s^{-1}, nearly twice the background speed. As f grows, the eddy shedding in the ABL becomes confined in a relatively narrow lee area laterally, with an enhanced small-scale structure; it develops faster and it is more unsteady, all when $f \neq 0$. With $Fr < 1$ the mentioned increase in \$ with f is now brought down close to the ABL and thus intensified. This in turn increases K_m and the TKE. The TKE fields corresponding to Figs. 7(c) and (d) and Figs. 8(c) and (d), being close enough to the wave breaking, are vertically more inhomogeneous than the specific humidity shown. These TKE fields exhibit elevated maxima similar to those in Enger and Grisogono (1998).

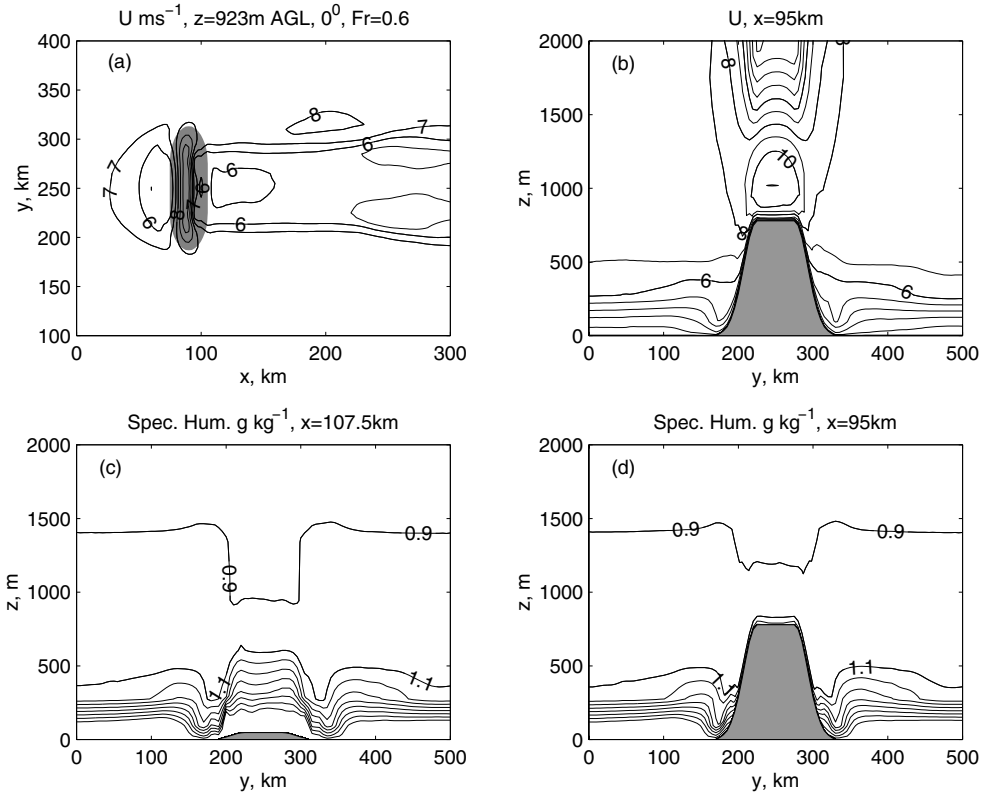

Figure 5. Similar to Fig. 1 but for $Fr = 0.6$ and in (a) at 923 m AGL. The flow is almost perfectly symmetric about $y = 250$ km, except for the moderate variations in the wave-breaking activity over the flanks, $y \approx 190$ km and 310 km. The vertical component, w, is in (c) $-4 < w \leqslant 8$ cm s^{-1}, and in (d) $-2 < w \leqslant 70$ cm s^{-1} (not shown).

It is only away from the wave-breaking areas that the TKE and specific humidity follow each other nicely.

Vorticity is an essential part of nonlinear dynamics. A full understanding of it in the presence of orographic-wave breaking and wakes is still under development, e.g. Smith and Smith (1995), Rotunno *et al.* (1999) and Hunt *et al.* (2001). Tilting of baroclinically generated vorticity is one way of producing counter-rotating vortices in the lee (vortex dipole) according to Hunt *et al.* (1997) and Rotunno *et al.* (1999); this is a totally different mechanism from vorticity production by friction via stresses acting on the flow at the mountain surface. Subgrid contributions to vorticity production are very important locally—where wave breaking occurs. Including f, the symmetry in the flow and the vortices is broken.

Vorticity is not clearly defined in non-orthogonal coordinates (e.g. as in the MIUU model), but it corresponds to that in the Cartesian system when computed over horizontal areas, i.e. away from the mountain here. (In this hydrostatic model with terrain slopes always less than 5°, the vertical vorticity component, ξ, is often similar in value to that in the Cartesian system even over slightly non-horizontal surfaces.) We discuss ξ only off the slopes, and it is computed here as in Kessler and Douglas (1991). Figures 9 and 10 show the absolute vorticity, $\xi + f$, and horizontal divergence, D, for $\phi = 0°$ and 45°, respectively, at two heights after 20 h. The (ξ, D) is diagnosed from the wind

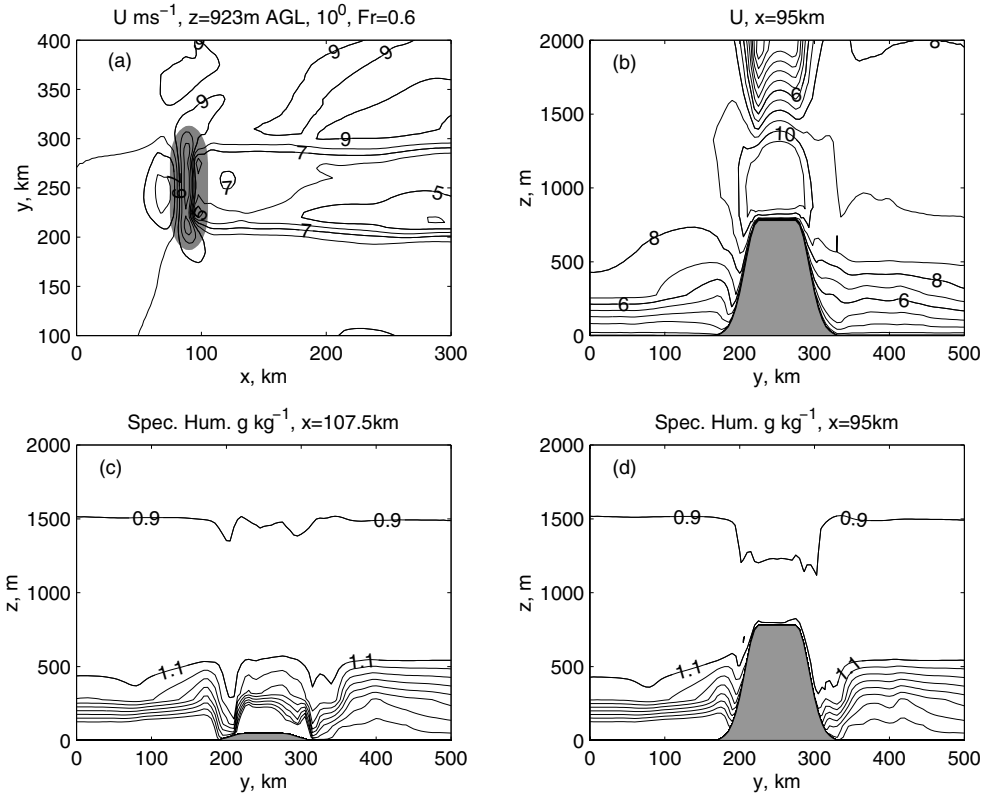

Figure 6. Same as Fig. 1 but for $Ro_x = 32$ ($\phi = 10°$). Note the moderate flow distortion compared to that in Fig. 5, e.g. in the upstream area, and in the lowest 500 m (in (b), (c) and (d)) applying to the bulk of the ABL. The vertical component, w, is (c) $-3 < w < 12$ cm s^{-1}, and (d) $0 \leqslant w \leqslant 70$ cm s^{-1} (not shown).

components (U, V). For $\phi = 0°$, ξ is dominated by relatively simple behaviour at both the heights. Behind the upstream blocking, the ξ banners stretch out in the lee linearly along the mean flow from the flanks (Fig. 9(a)), or as a horseshoe within the ABL relating to a single lee-vortex pair (Fig. 9(c)). The related D field follows in a similar way with a moderate contribution due to buoyancy waves for $x \geqslant 220$ km. Both ξ and D are rather coherent. On the other hand, ($\xi + f$, D) for $\phi = 45°$ shows multiple scales, see Fig. 10; clearly $\xi + f$ may become negative. Intensive small-scale vortex shedding is immersed into the already mentioned but now disturbed, main meandering banners embracing the lee area. At 923 m, such short intensive banners stretch out preferentially from left to right downstream, i.e. north-west to south-east (where the pressure is lowest), see Fig. 10(a). In the ABL, e.g. at 275 m (see Fig. 10(c)), the overall vortex shedding resembles a superposition of that in Figs. 10(a) and 9(c). With $\phi = 45°$ the whole range of values of ξ, or $\xi + f$ and D is more than doubled compared to those for $\phi = 0°$. A vigorous convergence–divergence pattern emanates most intensively off the flanks of h_M, where the wave breaking is most intensive. This is accentuated downstream of the northern flank where relatively higher speeds are obtained, feeding back to the mean flow and modifying the ξ and D fields. The northern-side banners continue to regenerate ξ and D far in the lee. The rest of the lee side generates the shortest but still intensive structures. The banners off the southern flank, being of intermediate sizes, propagate somewhat further downstream, supported by the main southern banner defining the lee

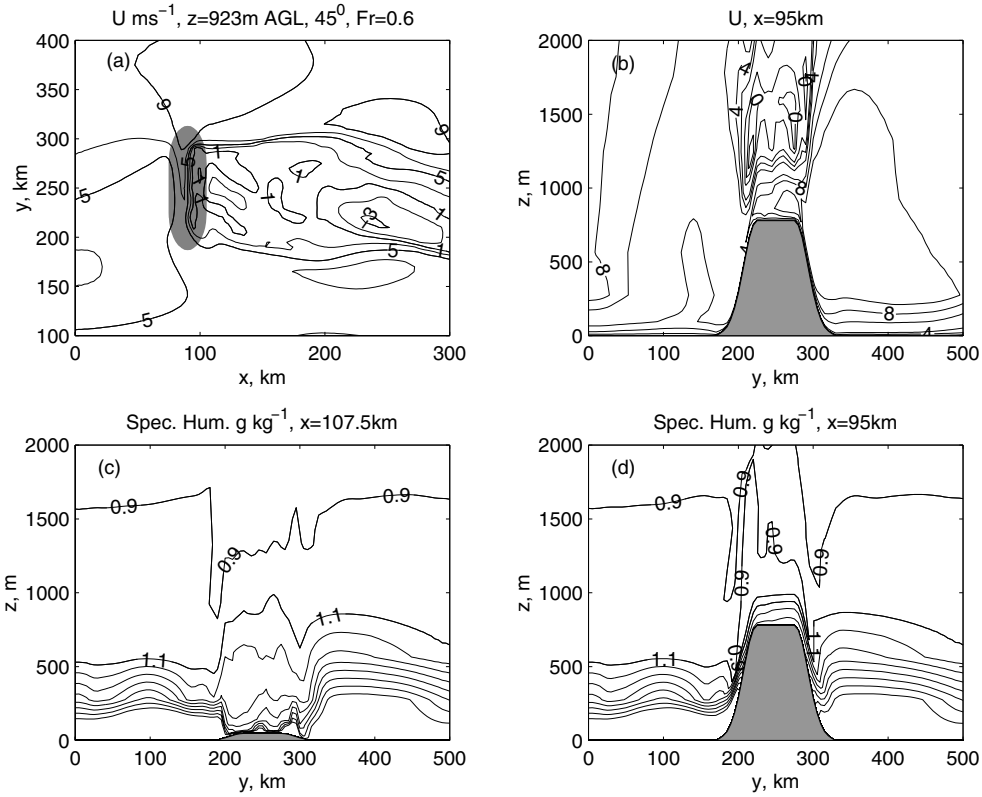

Figure 7. Same as Fig. 1 but for $Ro_x = 7.6$ ($\phi = 45°$). The isolines of U are at 2 m s^{-1} Intervals. The northern low-level jet (LLJ) with the wave breaking is the most prominent dynamic feature. The vertical component, w, is (c) $-7 < w < 20$ cm s^{-1}, (d) $-5 \leqslant w < 70$ cm s^{-1} (not shown).

edge there (near the southern LLJ). It appears that the most persistent 'ξ–D forcing' emanates from the northern flank in the lee going beyond L_R.

The vertical vorticity tendency is:

$$\xi_t = -(U\xi_x + V\xi_y + w\xi_z) - (f + \xi)(U_x + V_y) - (\Theta_x \Pi_y - \Theta_y \Pi_x) - (w_x V_z - w_y U_z) + (Ty_x - Tx_y), \quad (5)$$

where $(\ )_y \equiv \partial(\ )/\partial y$ etc. where the independent variables are the subscripts and Π is the Exner function. On the right-hand side of (5) the first term is the 3D advection, the second is the 'convergence', the third is the baroclinicity, the fourth is the tilting term and the fifth is the subgrid stress contribution, (Tx, Ty), to the ξ production. If (5) is written for ξ_t but without f and the result is subtracted from (5), a tendency equation for the vorticity difference between $f \neq 0$ and $f = 0$ is obtained, $Z_t \equiv \xi_{t,f} - \xi_{t,f=0}$. Our simulations show that within the first couple of hours, Z_t remains essentially close to zero as it is from the start. It is the (U, V) that is primarily affected by $f \neq 0$, which is qualitatively similar to the reasoning of Smith (1982), while the other fields, e.g. Π and Θ, are much less so. This idea agrees with the Θ fields for Figs. 5(b) to 8(b), exhibiting only small variations off the orography with respect to f (not shown). Meanwhile, the tilting is important over terrain slopes. If one assumes the solenoidal terms for $f \neq 0$ and f=0 mutually cancel in the equation for Z_t, which is partly based on Smith (1982)

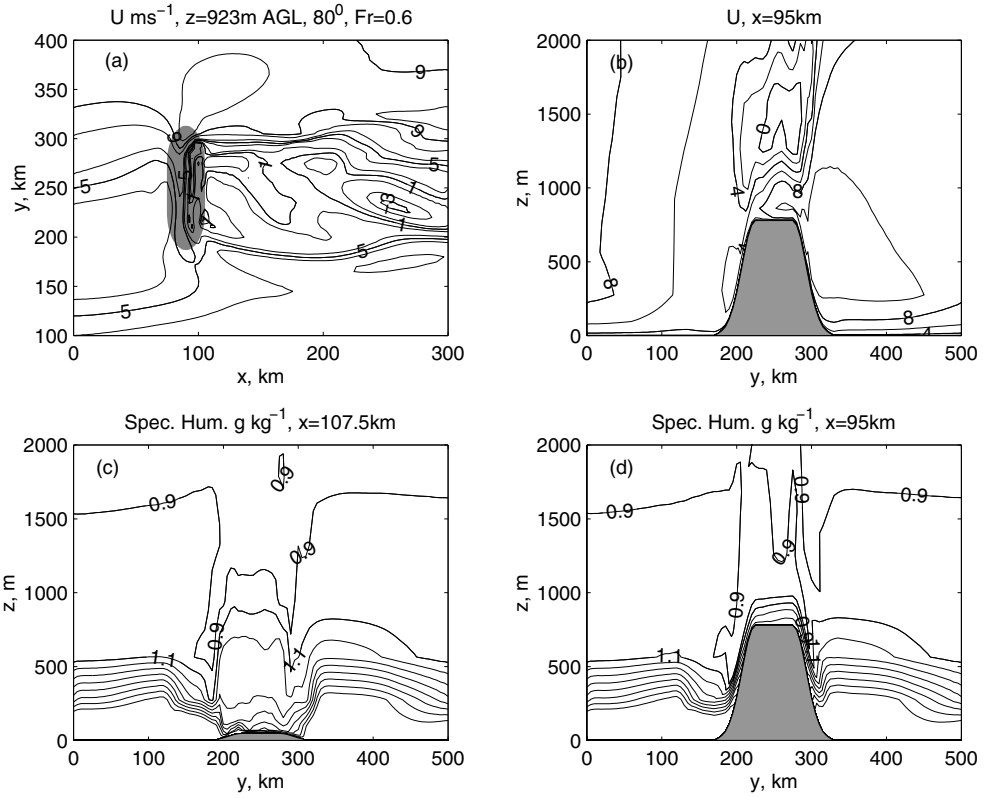

Figure 8. Same as Fig. 7 but for $Ro_x = 5.6$ ($\phi = 80°$). The northern LLJ is not only somewhat faster than that in Fig. 7 but also occupies a significantly larger domain here, thus it transports more momentum. In (c) $-10 < w < 24$ cm s^{-1}, and in (d) $-17 < w < 60$ cm s^{-1} (not shown).

and partly supported by the mentioned Θ fields, then a simplified nearly barotropic Z equation can be obtained. Namely:

$$(\mathrm{d}Z/\mathrm{d}t)_{f/2} = -Z\nabla_{\mathrm{H}} \cdot \mathbf{U}_{f/2} - f\nabla_{\mathrm{H}} \cdot \mathbf{U}_f - \mathit{retilt} - \mathit{resub}, \tag{6}$$

where $\mathbf{U} \equiv (U, V, w)$, ∇_{H} is the horizontal part of ∇, thus $D \equiv \nabla_{\mathrm{H}} \cdot \mathbf{U}$,

$$(\mathrm{d}/\mathrm{d}t)_{f/2} \equiv (\partial/\partial t + \mathbf{U}_{f/2} \cdot \nabla), \quad \mathbf{U}_{f/2} \equiv (\mathbf{U}_f + \mathbf{U}_{f=0})/2, \tag{7}$$

where *retilt* and *resub* are equal to the tilting difference and subgrid-stress contribution difference, respectively, between $\xi_{t,f}$ and $\xi_{t,f=0}$ (both *retilt* and *resub* are zero everywhere around $t = 0$). The appearance of f as a subscript shows its level of application, and is self-explanatory. If $\mathbf{U}$ varies relatively smoothly between $f = 0$ and $f > 0$, then both $\mathbf{U}$ in (6) can be expanded linearly as $\mathbf{U}_{f,0} = \mathbf{U}_{f/2} \pm \delta\mathbf{U}_{f/2}$ yielding

$$(\mathbf{U} \cdot \nabla\xi)_f - (\mathbf{U} \cdot \nabla\xi)_{f=0} \approx \mathbf{U}_{f/2} \cdot \nabla Z, \tag{8}$$

thus giving the advective part of the left-hand side of (6). Again, since Z is zero from the start, the only permanent non-zero forcing term in (6) is the second term on the right-hand side contributing to Z_t as $(Z_t)_f \equiv Z_F \equiv -f\nabla_{\mathrm{H}} \cdot \mathbf{U}_f = -fD$. Later on as the flow evolves, the other terms in (6) also contribute to Z_t and feed back to Z and D. However, the 'convergence' term due to the interaction between planetary

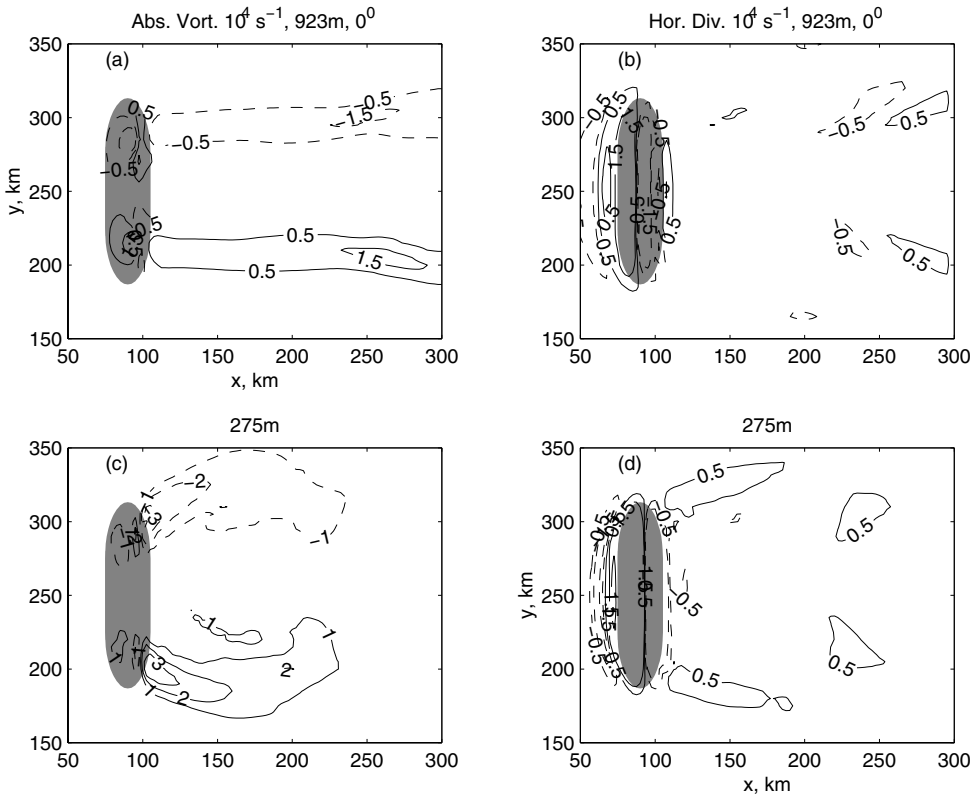

Figure 9. For Froude number $Fr = 0.6$ and latitude $\phi = 0°$ after 20 h: (a) vertical absolute vorticity, $(\xi + f)$ at height $z = 923$ m, and (b) horizontal divergence, D $(\times 10^4 \mathrm{s}^{-1})$, at $z = 923$ m; (c) and (d), as (a) and (b), respectively, but at $z = 275$ m. Zero-contours are suppressed, isoline interval is 10^{-4} s^{-1}, negative values are dashed. Note the more linear patterns in (a) and (b) with 'horseshoe' patterns in (c) and (d). The orography is light grey. Away from the orography values barely exceed $\pm 2f$.

vorticity f and mesoscale horizontal divergence D, orographically induced, is of the utmost importance for the production of $\xi_f = \xi_{f=0} + Z$ in this flow regime. The Z field looks similar to ξ_f shown in Fig. 10. For curiosity, the argument about $Z_F = -fD$ is mathematically similar to simplified potential-vorticity conservation; here ξ is clearly not conserved. However, the main forcing of the vorticity difference, Z, behaves as this simplified conservation law.

As ξ in (5), D can also be manipulated to obtain the tendency for the horizontal divergence difference, $\Delta \equiv D_f - D_{f=0}$, similar to Z and (6). With the same assumptions as for Z, Δ_t is most permanently driven by $(\Delta_t)_f \equiv \Delta_F \equiv f\xi$. The simplified forcing coupling presented, between $\xi_{t,f}$ and $D_{t,f}$, or Z_F and Δ_F, via $-fD$ and $f\xi$, respectively, emphasizes the nonlinear interaction in the mesoscale (ξ, D) field in the presence of the planetary vorticity related to the DRP. This primary negative wave-like feedback, provided by the wave breaking and f, is responsible for the enhanced small-scale variability in the lee, see Fig. 10. Of course, such a dynamic interplay as the DRP is trivially absent in both the case where $f = 0$ (Figs. 5 and 9), and in wave-breaking free flows (Figs. 1 to 4). It is through the presence of rotation that the 3D dynamics is coupled more efficiently, passing the wave-breaking information between ξ and D via f, Figs. 6, 7, 8, and 10.

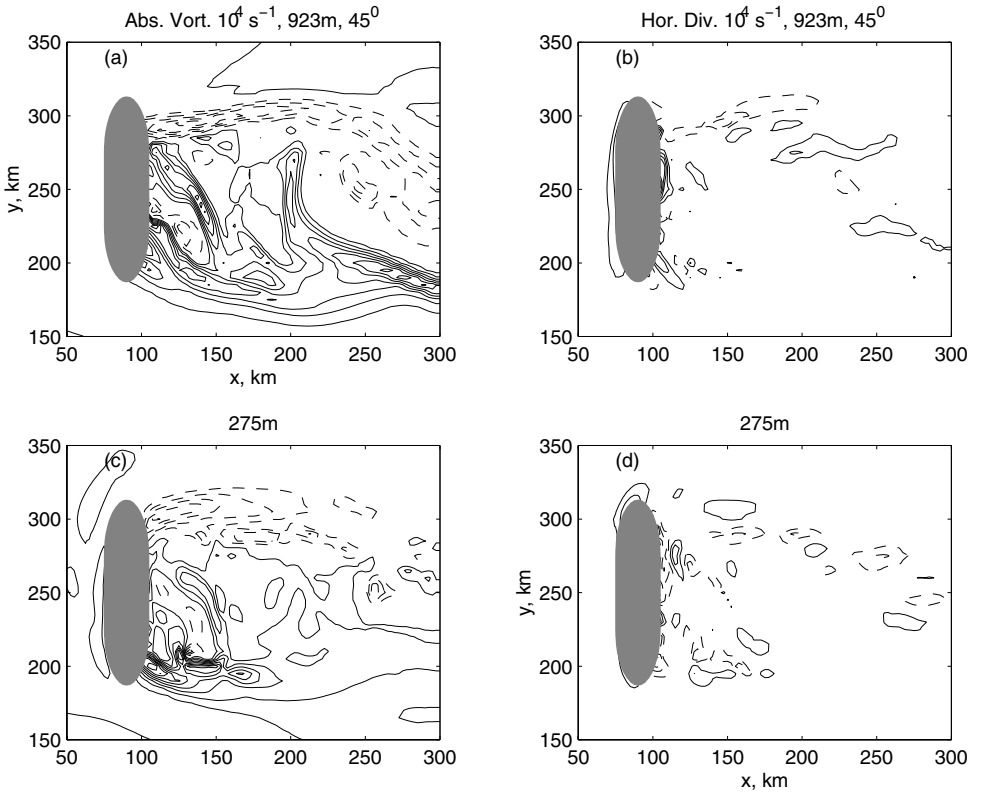

Figure 10. Same as Fig. 9 but for $\phi = 45°$. Note the intensive small scales embedded in the larger scale confining the lee; here the ranges of $|\xi + f|$ and $|D|$ are more than twice those in Fig. 9 with lee-extremes exceeding several $|f|$. Positive values (solid lines) start from 10^{-4}s^{-1}.

One could come to similar conclusions on what dominates the significant ξ differences at various latitudes in an even more plausible, simplistic way. The only term absent in $\xi_{t,f=0}$ but present in (5) for $\xi_{t,f}$ is $Z_F = -fD$, i.e. the part of the 'convergence term' due to the presence of f in the terrain-induced divergence–convergence pattern, D. The latter is dominated by: (i) the overall flow-splitting and blocking on the upwind side, and (ii) the wave breaking at the flanks and downslope side. This Z_F can be also written as $Z_F = +f\partial w/\partial z$ using the continuity and Boussinesq approximation. In our case, in the lee: $\partial U/\partial x \approx \Delta U/L_x \approx 8\ \text{m s}^{-1}/10^4\ \text{m} \approx 8 \times 10^{-4}\ \text{s}^{-1}$, or $\partial w/\partial z \approx |w|/(\lambda_z/2) \approx 1\ \text{m s}^{-1}/(1.9 \times 10^3\ \text{m}) \approx 5.3 \times 10^{-4}\ \text{s}^{-1}$, where the wave-breaking layer thickness and the vertical velocity are from the simulations, and also relate to Smith (1977). Thus, for $f = 10^{-4}\ \text{s}^{-1}$, $|Z_F|$ is about $5 - 8 \times 10^{-8}\ \text{s}^{-2}$ yielding after, say, 4 h, about $10^{-3}\ \text{s}^{-1}$ of new vorticity, positive or negative, which is a significant amount compared to f. The other terms seem to be a couple of times smaller, say within $\pm 3f$ values.

A similar argument applies to Δ_F. Once again, D is generally more vigorous on the northern lee (see Fig. 10), thus maintaining the more intensive $|\xi|$ production there and the consequent interplay between D and ξ. The cascade of scales, applying to both ξ and D, is a typical 3D feature in geophysical flows where the effects of rotation, no-slip lower boundary condition and turbulence are all considered, Fig. 10.

Finally, Z_F is formally the same governing term as in the simplified synoptic-scale vorticity equation (e.g. Holton 1992). The essential difference is in the synoptic and mesoscale vorticity/divergence dynamics there and here, respectively. Since the (ξ, D) production at the mountain lee occurs here over $2L_y \approx L_R$, stronger on one lee side and all in the presence of f, this production appears substantial and it dominates the flow over many L_R in the lee. This is a much stronger way that f affects buoyancy waves, i.e. via the DRP, than via linear superposition as for buoyancy–inertia waves.

(*d*) *ABL variations, Fr = 0.6*

Figure 11 shows the specific humidity at three different heights for the four values of ϕ in Table 1. The north–south symmetry around $y = 250$ km present for $Ro_x = \infty$ (see Figs. 11(a), (b) and (c)) is only moderately distorted at $\phi = 10°$ (Figs. 11(d), (g) and (j)) but progresses with larger ϕ (Figs. 11(g) to (l)). This relates to the distortion of the counter-rotating lee eddies, wave breaking and the upstream blocking. A new southern low-level maximum appears and strengthens with ϕ (Figs. 11(e), (g) and (j)) around $x \approx 100$ or 200 km, $y \approx 170$ km due to the preferential upstream advection. With height and ϕ, this area turns to the minimum while the northern flank becomes the maximum (Figs. 11(i), (k) and (l)) around $x \approx 80$ km, $y \approx 300$ km. The elevated lee-side maximum breaks off in the immediate lee, moves downstream and somewhat southward for about L_R (Figs. 11(h), (i), (j), (k) and (l)). The middle and upper ABL (see Figs. 11(b), (c), (e), (f), (h), (i), (k) and (l)) displaces the upstream maximum northward and slightly closer to the mountain with increasing ϕ, or decreasing Ro_x. The specific humidity of the middle and upper ABL moves qualitatively in accord with the simplified potential vorticity, $(\xi + f)/h \approx$ constant, acquiring an anticyclonic motion around the orography. On the other hand, this seems to be reversed in the lower ABL (Figs. 11(a), (d), (g) and (j)), thus suggesting a differential layering of the ABL north and south of the orography.

An additional spatio–temporal analysis suggests that for $Ro_x < \infty$ the northern eddy stretches out more, presumably draining energy from the northern LLJ, while the related southern eddy shrinks. Meanwhile, the southern low-level high humidity plunges into the lee further downstream in a re-generated, new (more intensive) southern eddy (close to the southern LLJ). The latter meets and disturbs a part of the northern lee eddy, and the 3D eddy-shedding continues leaving the model domain. The finding of Hunt *et al.* (2001) that the air flow rises on the left and descends on the right of the mountain exposed to a westerly flow in the northern hemisphere appears correct; yet in the lee there is no steady state as the 3D eddies are shed and interact with the surrounding, especially with the LLJ on both sides. Hence, the associated lee-side ABL varies significantly.

Several (y, z) cross-sections for $\phi = 45°$ are shown in Fig. 12 taken 60 and 160 km downstream from the mountain top, i.e. $x = 150$ and 250 km, respectively, showing *TKE*, λ_{turb}, vertical velocity, w, and the specific humidity. The ABL is horizontally inhomogeneous over at least a few L_R away from the orography. The northern lee ABL contains roughly twice the TKE than its southern counterpart (Figs. 12(a), (b), (c) and (d)), and its specific humidity is more mixed vertically. Hence, the humidity supply to the eddy-shedding area, roughly $200 \leqslant y \leqslant 300$ km, comes more from the southern than the northern side (Figs. 12(g) and (h)). These asymmetric distributions can have important consequences on the low-level cloud formation and air chemistry. The eddy-shedding area, due to substantial horizontal shears, generates vertical motions of up to several cm s^{-1} (Figs. 12(e) and (f)). These produce vertically propagating transient buoyancy waves that weakly interact with the orographic waves aloft, modulating their elevated parabolically shaped wave-pattern (not shown). Compared to Fig. 7 in the

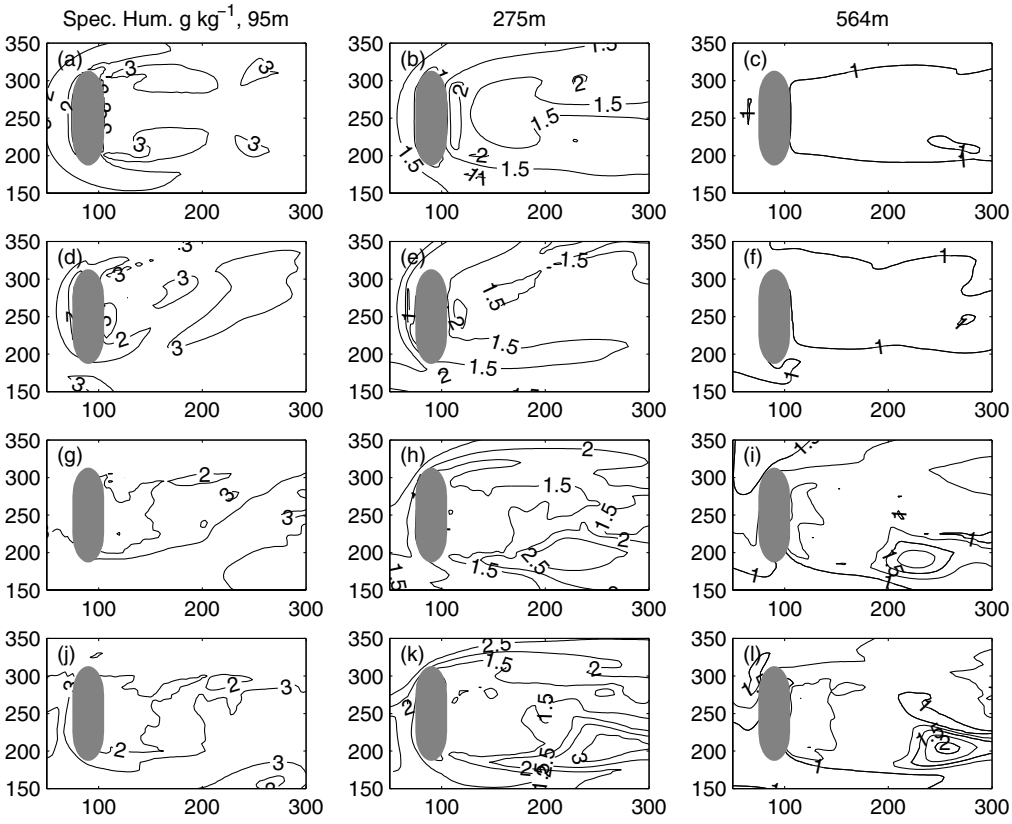

Figure 11. The specific humidity (g kg^{-1}) corresponding to Figs. 5, 6, 7 and 8, with Froude number, $Fr = 0.6$, after 20 h: (a) horizontal cross-section at 95 m for latitude $\phi = 0°$ (isolines are at 1 g kg^{-1} intervals), (b) horizontal cross-section at 275 m for $\phi = 0°$ (isolines at 0.5 g kg^{-1} intervals), (c) horizontal cross-section at 564 m for $\phi = 0°$ (isolines at 0.25 g kg^{-1} intervals); (d), (e) and (f) are as (a), (b) and (c), respectively, but for $\phi = 10°$; (g), (h) and (i) are as (a), (b) and (c), respectively, but for $\phi = 45°$; (j), (k) and (l) are as (a), (b) and (c), respectively, but for $\phi = 80°$. The symmetry around $y = 250$ km, present for $\phi = 0°$ (see (a) (b) and (c)) is broken with increased latitude. The overall atmospheric boundary-layer horizontal mixing decreases with increasing ϕ, hence the larger range of the humidity values at larger ϕ. The orography is as in Fig. 1.

immediate lee, here h recovers being ≈ 600 m for the southern ABL and a few hundreds of metres higher for the northern ABL. This h disagrees with h_{TKE} only in the lee (compare Figs. 12(a) and (b) with Figs. 12(g) and (h)).

(*e*) *Additional remarks*

One test run was made with a very stretched horizontal grid, more than five times larger in the x direction and two times larger in the y direction (1600 km, 1200 km): 2.5 km $\leqslant \Delta x <$ 45 km, 5 km $\leqslant \Delta y <$ 27 km. The rest is as in $(Fr, \phi) = (0.6, 45°)$. The estimation of the length of the wake effect, related to the 'spin-down process' and addressed in Hunt *et al.* (2001), $x_w \approx$ O(1000 km), agrees with our results*. This is illustrated in Fig. 13. Due to the gradual deterioration of the horizontal resolution, the eddies' fine structure from Fig. 11 is lost in Fig. 13; nonetheless, it is clear that the eddy-perturbations approach the model boundary 900 km downstream from the

* There is a transcription error in their u_* estimating δ towards the foot of page 630; it should read $u_* \approx 0.1$ m s^{-1} with respect to the other parameters.

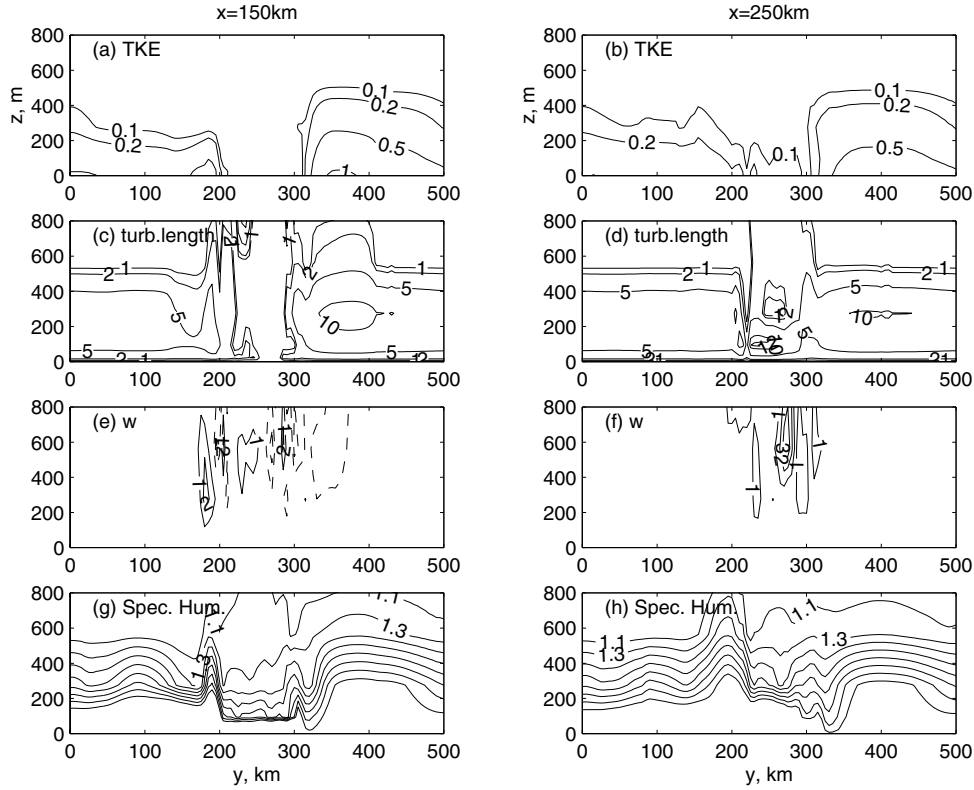

Figure 12. Vertical cross-sections for Froude number $Fr = 0.6$ and latitude $\phi = 45°$, 60 km and 160 km downstream from the mountain top at $x = 90$ km showing: (a) turbulent kinetic energy (*TKE*, $m^2 s^{-2}$) at $x = 150$ km, (b) *TKE* at $x = 250$ km; (c) and (d) as (a) and (b) but for turbulent length scale (λ_{turb}, m); (e) and (f) as (a) and (b) but for vertical velocity (w, cm s^{-1}) where dashed lines are negative; (g) and (h) as (a) and (b) but for specific humidity (g kg^{-1}). Besides the deeper northern than southern atmospheric boundary layer (ABL), there is a variation in the ABL differential layering. The eddy area has the most variable ABL, roughly $200 < y < 300$ km, with significant velocity perturbations.

mountain top. When the same run is performed with $f = 0$, the range of the (U, V) values is moderately and significantly smaller than in Figs. 13(a) and (b), respectively. This yields the longer eddy-shedding distance and the more inhomogeneous ABL in Fig. 13 than for $f = 0$ which stretches up to $x_w \approx 600$ km, with a thinner and weaker eddy-shedding region (not shown) for the parameter space studied. Yet another run with $(Fr, \phi) = (0.6, 45°)$ is made, but starting with $U = -8$ m s^{-1}. The equivalent results and the DRP at work are found as in e.g. Figs. 7 and 10, but now maximizing the flow over the southern flank and all being symmetrically the opposite. Thorpe *et al.* (1993) showed modelling and observational evidence for potential-vorticity anomalies due to the Alps and the related ABL, all for a special synoptic set-up; these anomalies were advected far away from the Alps, thus resembling qualitatively the findings discussed here. However, the synoptic set-up in Thorpe *et al.* (1993) differs from ours and a closer relation does not seem possible.

Apparently, the ABL top based on the TKE, h_{TKE}, works fine except in the vicinity of wave breaking, where a secondary max(*TKE*) occurs aloft at around $\lambda_z/2$ (Smith 1977; Grisogono 1995; Enger and Grisogono 1998). If these TKE maxima are h_{TKE}

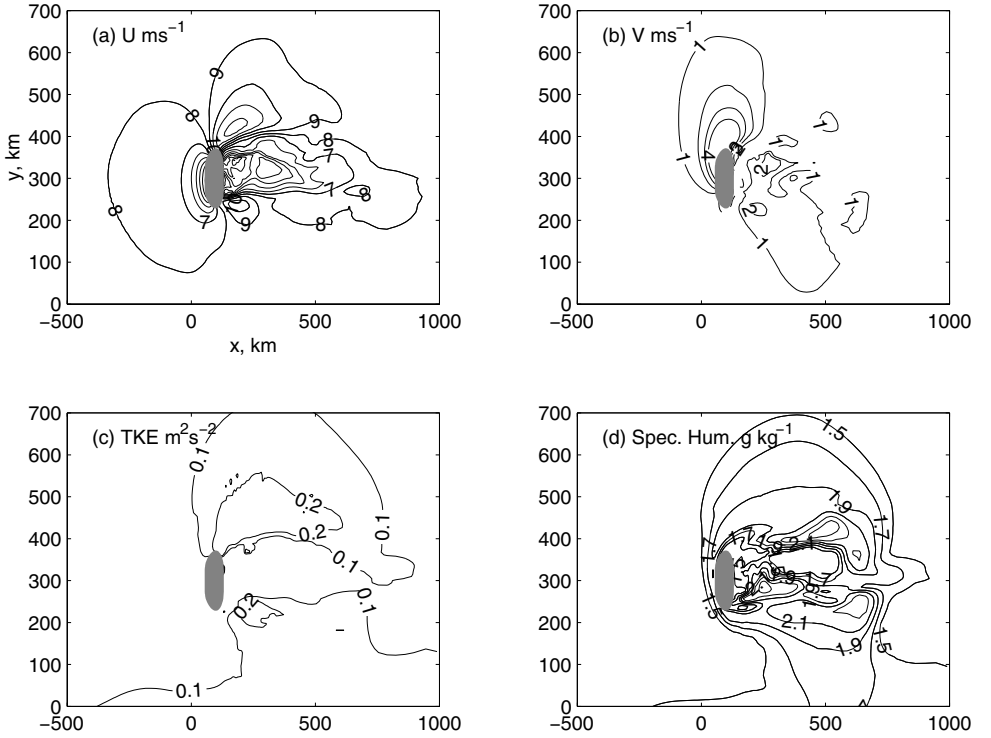

Figure 13. A horizontally stretched domain, otherwise like the run with Froude number $Fr = 0.6$ and latitude $\phi = 45°$, shown at 275 m after 20 h: (a) easterly velocity component (U, m s^{-1}), (b) northerly component (V, m s^{-1}), (c) the turbulent kinetic energy (TKE, m^{-2}s^{-2}), and (d) the specific humidity (g kg^{-1}). The resolution gradually decreases from the centre toward the lateral boundaries. The orography contours (light grey) are thus slightly distorted compared to the previous figures. The perturbations stretch out of the domain, $x_{MAX} = 1000$ km, under dispersion and dissipation. Here the max(TKE) $\leqslant 0.5$ m^{2}s^{-2} is 50% higher than for the respective Coriolis force $f = 0$ run (not shown).

or more apart, which is common, this ABL top estimation becomes meaningless and probably also the very concept of a more classic ABL.

4. Conclusions

Using a 3D mesoscale numerical model, the ABL response to orographic forcing in the presence of $f \neq 0$, is studied. This relates to (Fr, Ro) parameter space. Two sets of simulations are presented, weakly nonlinear and strongly nonlinear; within each only latitude varies, $\phi = 0$, 10, 45 and 80°N having $Ro_x = \infty$, 32, 7.6 and 5.6. The nonlinear flow approaches, goes around and partly over the terrain with a preference for the northern-side, and all under wave breaking. The orographic-wave breaking occurring for $Fr < 1$, affected by $f > 0$, intensifies on the northern flank for the westerly flow (Figs. 5 to 8) as also found in other studies. Breaking the flow symmetry around the orography (the integral/cumulative effect) changes the (ξ,D) fields thus lifting the northern ABL, modulating eddy shedding and turbulence thus leading to a differential layering of the ABL (the secondary effect). The northern LLJ is stronger and more stretched out than its southern counterpart. Their unsynchronized meandering, together with the asymmetric wave breaking over $2L_y \approx L_R$, induces strong fluctuations in the (ξ, D) field.

The pattern of (ξ, D) is altered in structure and enhanced in amplitude (more than doubled) for $1 < Ro_x \ll \infty$, $Fr < 1$ compared to the irrotational case. The responsible agent is the strong coupling between the $-fD$ and $f\xi$ terms in the production of (ξ, D). This production is significant as it occurs over $2L_y \approx L_R$. It not only causes the lifting of the northern and the lowering of the southern side of the ABL, as found by Hunt *et al.* (2001), but also an overall differential layering of the ABL. One may speak of two interrelated 'resonances' here: the enhanced (ξ, D) production due to wave breaking (the primary atmosphere–orography resonance) taking place in the presence of f (the secondary resonance); the former resonance is mainly in the vertical, and the latter in the horizontal plane. The resonances cannot independently produce the ABL's differential layering; the primary, 'vertical' resonance must be induced, $Fr \leqslant 1$, so that the secondary, weaker, 'horizontal' one can also be triggered, $1 < Ro_x \ll \infty$, then jointly altering the ABL. This is called here the double-resonance phenomenon or DRP. In this way, effects of the initial mesoscale forcing, concentrated within L_R, may extend over the synoptic scale $\gg L_R$.

Mapping the LLJ north (stronger for $U > 0$ and $f > 0$) and south (weaker) of the orographic lee side, in relation to the differential layering of the ABL, indicates important possible consequences for tracers, clouds and air chemistry. The lee-side eddy-shedding ABL, having different wind shears at both its sides, induces significant variations in the TKE distribution which also alters the specific humidity which affects the formation of cloud.

If a numerical model does not simulate some of the important ingredients for the DRP properly, the lee-side prognostic fields will be in error. For instance, it is known that the LLJ is often poorly resolved in NWP models (e.g. Rogers *et al.* 1998), and features such as the LLJ may dominate flux properties of the lower troposphere (e.g. Mahrt 1998). Similar arguments apply to orographic-wave breaking. Since our current NWP and climate models have insufficient resolution and/or oversimplified turbulence parametrization schemes to simulate the DRP adequately, much of the related dynamics over complex terrain, stretching possibly even to the synoptic scale, can be erroneous.

Continuing from the work of Ólafsson (2000) and Hunt *et al.* (2001), the advancements in this study are as follows.

(i) The vertical vorticity and divergence field (ξ, D) is shown and discussed in a more interrelated, mutually generating way in the field of f; the interaction is called DRP. As the (ξ, D) generates wave breaking over $O(L_R)$, the mesoscale perturbations remain in the flow over a synoptic distance. This is an integral/cumulative effect.
(ii) The TKE and specific humidity for the fully inhomogeneous ABL is shown and discussed in terms of their generation and advection, respectively (the secondary, differential effect).

ACKNOWLEDGEMENTS

Ron B. Smith from Yale University, USA, is thanked for discussion and criticism during the early stage of this study. Matthias Mohr from Uppsala University is thanked for his technical support, as are Stefan Söderberg and Oskar Parmhed from Stockholm University for their comments. Valuable criticism from two anonymous reviewers and J. C. King, the associate Editor, are appreciated.

References

Abiodun, B. J. and Enger, L. 2002 The role of advection of fluxes in modelling dispersion in convective boundary layers. *Q. J. R. Meteorol. Soc.*, **128,** 1589–1608

Andrén, A. 1990 Evaluation of a turbulence closure scheme suitable for air-pollution applications. *J. Appl. Meteorol.*, **29,** 224–239

Arya, S. P. 1999 *Air pollution meteorology and dispersion*. Oxford University Press, London, UK

Baines, P. G. 1995 *Topographic effects in stratified flows*. Cambridge University Press, Cambridge, UK

Bauer, M. H., Mayr, G. J., Vergeiner, I. and Pichler, H. 2000 Strongly nonlinear flow over and around a three-dimensional mountain as a function of the horizontal aspect ratio. *J. Atmos. Sci.*, **57,** 3971–3991

Broad, A. S. 1999 Do orographic gravity waves break in flows with uniform wind direction turning with height? *Q. J. R. Meteorol. Soc.*, **125,** 1695–1714

Brzovic, N. 1999 Factors affecting the Adriatic cyclone and associated windstorms. *Contrib. Atmos. Phys.*, **72,** 51–65

Cui, Z., Tjernström, M. and Grisogono, B. 1998 Idealized simulations of atmospheric coastal flow along the central coast of California. *J. Appl. Meteorol.*, **37,** 1332–1363

Ding, L., Calhoun, R. J. and Street, R. L. 2003 Numerical simulation of strongly stratified flow over a three-dimensional hill. *Boundary-Layer Meteorol.*, **107,** 81–114

Durran, D. R. 1999 *Numerical methods for wave equations in geophysical fluid dynamics*. Springer, New York, USA

Egger, J. and Hoinka, K. P. 1992 Fronts and orography. *Meteorol. Atmos. Phys.*, **48,** 3–36

Enger, L. 1990 Simulation of dispersion in moderately complex terrain. Part A: The fluid dynamics model. *Atmos. Environ.* **24A,** 2431–2446

Enger, L. and Grisogono, B. 1998 The response of bora-type flow to sea surface temperature. *Q. J. R. Meteorol. Soc.*, **124,** 1227–1244

Epifanio, C. R. and Durran, D.R. 2001 Three-dimensional effects in high-drag-state flows over long ridges. *J. Atmos. Sci.*, **58,** 1051–1065

Fritts, D. C., Isler, J. R. and Andreassen, Ø. 1994 Gravity wave breaking in two and three dimensions. 2: Three-dimensional evolution and instability. *J. Geophys. Res.*, **99,** 8109–8123

Grisogono, B. 1995 Wave-drag effects in a mesoscale model with a higher-order closure turbulence scheme. *J. Appl. Meteorol.*, **34,** 941–954

Grisogono, B. and Oerlemans, J. 2002 Justifying the WKB approximation in pure katabatic flows. *Tellus*, **54A,** 453–463

Grisogono, B. and Tjernström, M. 1996 Thermal mesoscale circulations on the Baltic coast. Part II: Perturbation of surface parameters. *J. Geophys. Res.*, **101,** 18999–19012

Grubišic, V. and Smolarkiewicz, P. 1997 The effect of critical levels on 3D orographic flows: Linear regime. *J. Atmos. Sci.*, **54,** 1943–1960

Holmgren, P. 1994 An advection algorithm and an atmospheric airflow application. *J. Comput. Phys.*, **115,** 27–42

Holton, J. R. 1992 *An introduction to dynamic meteorology*. Third edition. Academic Press, San Diego, USA

Hunt, J. C. R., Stretch, D. D. and Britter, R. E. 1988 Length scales in stably stratified turbulent flows and their use in turbulence models. Pp. 285–321 in *Stably stratified flow and dense gas dispersion.* Ed. J. S. Puttock. Clarendon Press, Oxford, UK

Hunt, J. C. R., Feng, Y., Linden, P. F., Greenslade, M. D. and Mobbs, S. D. 1997 Low-Froude-number stable flows past mountains. *Il Nuovo Cimento*, **20,** 261–272

Hunt, J. C. R., Ólafsson, H. and Bougeault, P. 2001 Coriolis effects on orographic and mesoscale flows. *Q. J. R. Meteorol. Soc.*, **127,** 601–633

Ivancan-Picek, B. and Tutiš, V. 1996 A case study of a severe Adriatic bora on 28 December 1992. *Tellus*, **48A,** 357–367

Kessler, R. C. and Douglas, S. G. 1991 A numerical study of mesoscale eddy development over the Santa Barbara channel. *J. Appl. Meteorol.*, **30,** 633–651

Klemp, J. B. and Durran, D. R. 1987 Numerical modelling of Bora winds. *Meteorol. Atmos. Phys.*, **36,** 215–227

Klemp, J. B. and Lilly, D. K. 1978 Numerical simulation of hydrostatic mountain waves. *J. Atmos. Sci.*, **35,** 78–107

Lesieur, M. 1997 *Turbulence in fluids*. Third edition. Kluwer, Dordrecht, the Netherlands

Mahrt, L. 1998 Stratified atmospheric boundary layers and breakdown of models. *Theoret. Comput. Fluid Dyn.*, **11,** 263–279

Miranda, P. M. A. and James, I. N. 1992 Non-linear three-dimensional effects on gravity wave drag: Splitting flow and breaking waves. *Q. J. R. Meteorol. Soc.*, **118,** 1057–1081

Nappo, C. J. 2002 *An introduction to atmospheric gravity waves*. Academic Press, San Diego, USA

Ólafsson, H. 2000 The impact of flow regimes on asymmetry of orographic drag at moderate and low Rossby numbers. *Tellus*, **52A,** 365–379

Ólafsson, H. and Bougeault, P. 1996 Nonlinear flow past an elliptic mountain ridge. *J. Atmos. Sci.*, **53,** 2465–2489

1997 The effect of rotation and surface friction on orographic drag. *J. Atmos. Sci.*, **54,** 193–210

Overland, J. E. 1984 Scale analysis of marine winds in straits and along mountainous coasts. *Mon. Weather Rev.*, **112,** 2532–2536

Pedlosky, J. 1987 *Geophysical fluid dynamics*. Second edition. Springer-Verlag, New York, USA

Peltier, W. R. and Clark, T. L. 1979 The evolution and stability of finite-amplitude mountain waves. Part II: Surface wave drag and severe downslope windstorms. *J. Atmos. Sci.*, **36,** 1498–1529

Pierrehumbert, R. T. and Wyman, B. 1985 Upstream effects of mesoscale mountains. *J. Atmos. Sci.*, **42,** 977–1003

Rogers, D. P., Dorman, E. C., Edvards, K. A., Brooks, I. M., Melville, W. K., Burk, S. D., Thompson, W. T., Holt, T., Ström, L. M., Tjernström, M., Grisogono, B., Bane, J. M., Nuss, W. A., Morley, B. M. and Schanot, A. J. 1998 Highlights of coastal waves 1996. *Bull. Am. Meteorol. Soc.*, **79,** 1307–1326

Rotunno, R., Grubišic, V. and Smolarkiewicz, P. K. 1999 Vorticity and potential vorticity in mountain wakes. *J. Atmos. Sci.*, **56,** 2796–2810

Schär, C. and Durran, D. R. 1997 Vortex formation and vortex shedding in continuously stratified flows past isolated topography. *J. Atmos. Sci.*, **54,** 534–554

Schär, C. and Smith, R. B. 1993 Shallow-water flow past isolated topography. Part II: Transition to vortex shedding. *J. Atmos. Sci.* **50,** 1341–1412

Schumann, U. and Gerz, T. 1995 Turbulent mixing in stably stratified shear flows. *J. Appl. Meteorol.* **34,** 33–48

Shutts, G. J. 1998 Stationary gravity wave structure in flows with directional wind shear. *Q. J. R. Meteorol. Soc.*, **124,** 1421–1442

Smith, R. B. 1977 The steepening of hydrostatic mountain waves. *J. Atmos. Sci.*, **34,** 1634–1654

1980 Linear theory of stratified hydrostatic flow past an isolated mountain. *Tellus*, **32,** 348–364

1982 Synoptic observations and theory of orographically disturbed wind and pressure. *J. Atmos. Sci.*, **39,** 60–70

1985 On severe downslope winds. *J. Atmos. Sci.*, **42,** 2597–2603

1987 Aerial observations of the Yugoslavian Bora. *J. Atmos. Sci.*, **44,** 269–297

1989 Hydrostatic airflow over mountains. *Adv. Geophys.*, **31,** 1–41

Smith, R. B. and Grønås, S. 1993 Stagnation points and bifurcation in 3-D mountain airflow. *Tellus*, **45A,** 28–43

Smith, R. B. and Smith, D. F. 1995 Pseudo-viscid wake formation by mountains in a shallow-water flow with drifting vortex. *J. Atmos. Sci.*, **52,** 436–454

Stull, R. B. 1988 *An introduction to boundary layer meteorology*. Kluwer Academic Publishers, Dordrecht, the Netherlands

Söderberg, S. and Tjernström, M. 2002 Diurnal cycle of supercritical along-coast flows. *J. Atmos. Sci.*, **59,** 2615–2624

Thompson, R. S., Shipman, M. S. and Rottman, J. W. 1991 Moderately stable flow over a three-dimensional hill. *Tellus*, **43A,** 49–63

Thorpe, A. J., Volkert, H. and Heimann, D. 1993 Potential vorticity of flow along the Alps. *J. Atmos. Sci.*, **50,** 1573–1590

Tjernström, M. 1993 Turbulence length scales in stably stratified free shear flow analyzed from slant aircraft profiles. *J. Appl. Meteorol.*, **32,** 948–963

Tjernström, M. and Grisogono, B. 1996 Thermal mesoscale circulations on the Baltic coast. Part I: A numerical case study. *J. Geophys. Res.*, **101,** 18979–18997

2000 Simulations of super-critical flow around points and capes in a coastal atmosphere. *J. Atmos. Sci.*, **57,** 108–135

Tjernström, M., Enger, L. and Andrén, A. 1988 A three-dimensional numerical model for studies of atmospheric flows on the meso-g scale. *J. Theor. Appl. Mech.*, **7,** 167–194

Trüb, J. and Davies, H. C. 1995 Flow over a mesoscale ridge: Pathways to regime transition. *Tellus*, **47A,** 502–524